Barker, P.F., Camerlenghi, A., Acton, G.D., and Ramsay, A.T.S. (Eds.)
Proceedings of the Ocean Drilling Program, Scientific Results Volume 178

24. Data Report: Fine-Fraction Grain-Size Distribution Data and Their Statistical Treatment and Relation to Processes, Site 1095 (ODP Leg 178, Western Antarctic Peninsula)[1]

T. Moerz[2] and T.C.W. Wolf-Welling[3]

ABSTRACT

Fine-fraction (<63 µm) grain-size analyses of 530 samples from Holes 1095A, 1095B, and 1095D allow assessment of the downhole grain-size distribution at Drift 7. A variety of data processing methods, statistical treatment, and display techniques were used to describe this data set. The downhole fine-fraction grain-size distribution documents significant variations in the average grain-size composition and its cyclic pattern, revealed in five prominent intervals: (1) between 0 and 40 meters composite depth (mcd) (0 and 1.3 Ma), (2) between 40 and 80 mcd (1.3 and 2.4 Ma), (3) between 80 and 220 mcd (2.4 and 6 Ma), (4) between 220 and 360 mcd, and (5) below 360 mcd (prior to 8.1 Ma).

In an approach designed to characterize depositional processes at Drift 7, we used statistical parameters determined by the method of moments for the sortable silt fraction to distinguish groups in the grain-size data set. We found three distinct grain-size populations and used these for a tentative environmental interpretation. Population 1 is related to a process in which glacially eroded shelf material was redeposited by turbidites with an ice-rafted debris influence. Population 2 is composed of interglacial turbidites. Population 3 is connected to depositional sequence tops linked to bioturbated sections that, in turn, are

[1]Moerz, T., and Wolf-Welling, T.C.W., 2001. Data report: Fine-fraction grain-size distribution data and their statistical treatment and relation to processes, Site 1095 (ODP Leg 178, western Antarctic Peninsula). *In* Barker, P.F., Camerlenghi, A., Acton, G.D., and Ramsay, A.T.S. (Eds.), *Proc. ODP, Sci. Results,* 178, 1–27 [Online]. Available from World Wide Web: <http://www-odp.tamu.edu/publications/178_SR/VOLUME/CHAPTERS/SR178_24.PDF>. [Cited YYYY-MM-DD]
[2]GEOMAR Research Center for Marine Geoscience, Wischhofstrasse 1-3, C4, 24148 Kiel, Federal Republic of Germany. **tmoerz@geomar.de**
[3]Institute for Geosciences, Christian-Albrechts University Kiel, Olshausenstrasse 40, 24118 Kiel, Federal Republic of Germany.

Initial receipt: 16 April 2001
Acceptance: 8 August 2001
Web publication: 29 November 2001
Ms 178SR-234

influenced by contourite currents and pelagic background sedimentation.

INTRODUCTION

The area west of the Antarctic Peninsula is a key region for studying and understanding the history of glaciation in the southern high latitudes during the Neogene. The area is critical for learning variations in the western Antarctic continental ice sheet, the sea ice cover, the induced eustatic sea level change, and consequences for the global climatic system. Sites 1095, 1096, and 1101 (Fig. F1) were drilled on sediment drifts that form the continental rise to examine the nature and composition of sediments deposited under the influence of the fluctuating Antarctic Peninsula ice sheet. The ice sheet has repeatedly advanced to the shelf edge and subsequently released glacially eroded material on the continental slope and rise (Barker, 1995; Barker et al., 1998, 1999). Mass-wasting processes on the slope are responsible for downslope sediment transport by turbidity currents within a channel system between the drifts (Rebesco et al., 1998). Bottom currents redistribute the sediments, thus leading to the final buildup of drift bodies (Camerlenghi et al., 1997). The high-resolution sedimentary sequences on the continental rise can be used to document the variability of continental glaciation and, therefore, allow us to assess the main factors that control sediment transport and depositional processes during glacial periods and their relationship to glacioeustatic sea level changes.

This research was carried out on material from Site 1095, where coring recovered sediments as old as late Miocene (9.7 Ma). Site 1095 lies in 3840 m of water in a distal position on the northwestern lower flank of Drift 7 (Fig. F2). We measured the grain-size distribution of 530 samples from Holes 1095A, 1095B, and 1095D to obtain a more detailed picture of three controlling factors: (1) the variability and magnitude of turbidites, (2) deep-oceanic currents (contourite currents), and (3) the ice-rafting component since the late Miocene.

METHODS

Sample Preparation

Sediment samples were taken from Site 1095 cores using a 10- to 20-cm³ plugging device. After freeze-drying, the sample was split by wet sieving into the fine (<63 µm) and coarse (>63 µm) fractions. The coarse fraction was oven dried, balanced, and set aside for further analysis (the results of the coarse-fraction analysis are given in the data report by Wolf-Welling et al., Chap. 21, this volume).

The water content of the suspended fine-fraction sample was reduced in two steps, by settling and the subsequent removal of excess water (by vacuum pump). We added H_2O_2 to remove remaining organic complexes (Anderson, 1963; Matthews, 1991) and rinsed the fraction with distilled water before a final removal of excess water. Na_2PO_4 was used as a final dispersant to avoid fine-particle clogging (McCave, 1995a; McCave et al., 1986). The final preparation step included 24-hr shaking in a overturn shaker and 1 hr in an ultrasonic bath directly before sample analysis (Fig. F3).

F1. Bathymetric map of the continental margin west of the Antarctic Peninsula, p. 11.

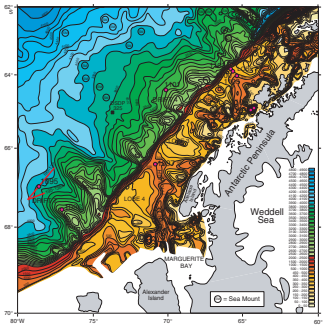

F2. Multichannel reflection seismic profile across the seaward end of Drift 7, p. 12.

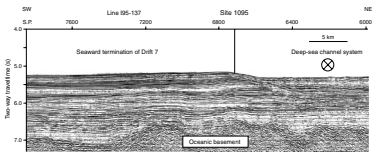

F3. Sample preparation scheme, p. 13.

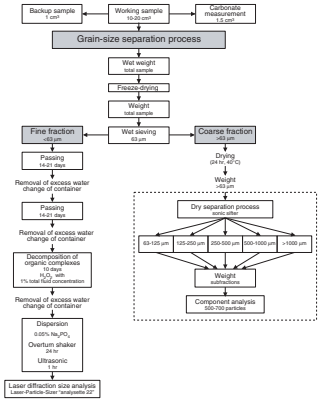

Laser Diffraction Analysis

The fine fraction was subsequently analyzed by laser diffraction. Measurements were carried out using the laser particle sizer "Analysette 22"-Economy (Fritsch GmbH Laborgerätebau, 1994) (Fig. F4A). The unit is equipped with a 632.8-nm wavelength and a 3-mW helium-neon laser and handles suspensions with a particle size between 0.1 and 600 µm. The laser analyzer consists of four components: a dispersion unit, the measuring cell and laser, a multielement detector, and a personal computer with software for recalculation and data display. The sample is fed into the dispersing and homogenization unit, which is equipped with an ultrasonic bath and a stirring compound. An interactive sample input, controlled by frequent absorption measurements, assures a certain grain-density range within the measuring cell. A centrifugal pump supports the transport of the sample to and from the measuring cell. After each measurement, the laser analyzer was set to rinse and clean the cell four times with distilled water.

The laser measurement itself is based on the sensory interpretation of Frauenhofer interference images produced by the scattering of monochromatic light on spherical grain boundaries (Von Bernuth, 1988). The size of the grains is related to wavelength and frequency (f), a geometry factor (k), and the radius of the first-order Frauenhofer interference ring (R_O) (Fritsch GmbH Laborgerätebau, 1994):

$$\text{Particle size} = (k \cdot f \cdot \text{wavelength})/R_o.$$

Particle sizes down to 0.02 µm can still be detected with sufficient accuracy using the Frauenhofer theorem (Von Bernuth, 1988). A special feature of this laser analyzing system is a fixed-focus optical setup with no focusing lenses behind the sampling cell, in contrast to other systems that use focusing lenses behind the sampling cell. In order to detect a wide range of particle sizes, the distance from sampling cell to the multimeter detector is variable (Fig. F4B, F4C). Shifting the sampling cell relative to the detector changes the diffraction angle and the size of the affected sensor area. A large distance between the sampling cell and detector therefore permits the measurement of larger particles with a smaller diffraction angle, and short distances are used for small particles with a wide diffraction angle (Fig. F4B, F4C) (McCave et al., 1986). Our fine-fraction data set consists of 31 size classes ranging from 0.425 to 63.314 µm. The size classes are given in Table T1. The size range of 0.4–63.3 µm was measured with a constant cell-to-detector spacing (single-range measurement). Since some of the plots displayed in this report are given in linear scale and others (e.g., the statistical moment plots) in ϕ units, we added a figure to demonstrate the relation between both scales (Fig. F5A) and the effects on the appearance of frequency distribution plots given in millimeter and ϕ values (Fig. F5B, F5C).

Stratigraphy and Age Model

The age model and stratigraphy for Site 1095 is based on the magnetostratigraphic results published in "Magnetostratigraphy" in Shipboard Scientific Party (1999b).

We assigned ages for each sample assuming linear sedimentation rates between age dates. Even though depth below seafloor and recovery-corrected depth values do not differ significantly, we decided to work with meters composite depth (mcd). Because of the small overlap

F4. Layout of the laser particle sizer, p. 14.

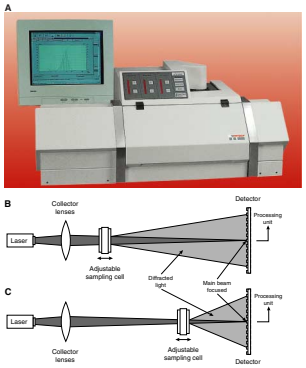

T1. Grain-size classes, p. 27.

F5. Size classes and differences in frequency spectra plots, p. 15.

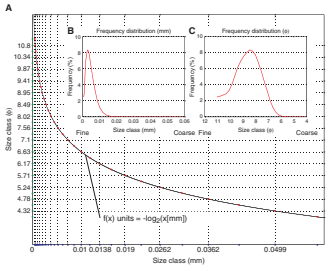

between Holes 1095A, 1095B, and 1095D, we do not expect important changes for our model compared to stratigraphically spliced depth scales. We excluded two samples in the overlapping part of Holes 1095A and 1095B (between 83.0 and 87.3 meters below seafloor) to avoid assigning overlapping ages to samples.

The hiatus at ~60 mcd discussed by Hillenbrand and Ehrmann (**Chap. 8,** this volume) and in "Magnetostratigraphy" and "Seismic Stratigraphy" in Shipboard Scientific Party (1999b) has not been considered in our age model. Even so, the data presented supports the ideas presented in Shipboard Scientific Party (1999b) and Hillenbrand and Fütterer (**Chap. 23,** this volume).

RESULTS

To provide a simplified overview of the fine-fraction grain-size frequency distribution of the data set, we have chosen a three-dimensional contour presentation that incorporates all samples with their individual frequency distributions (Fig. **F6**). The original data set was gridded to a 1-m depth and 20-k.y. age grid resolution, with linear interpolated size classes of the original 31 channels in micrometers. We applied a true two-dimensional zero-phase filter algorithm to smooth the data (the moving average filter has a size of five data points for the age or depth axis and three points for the grain-size axis). The contour algorithm is linear and resolves six levels representing the percent of sediment found for each grain-size class. Percent values refer to the total sediment sample dry mass. The >63-µm size fraction was added as an undifferentiated two-dimensional summary curve at the right side of the graph. Single data values and a zero-phase filtered curve, obtained with a one-dimensional filter (five point) of the same size as for the fine fraction, are given. The fine-fraction and smoothed coarse-fraction data are therefore in phase and have identical interpolated depth resolutions.

F6. Contour plots of the fine-fraction data, p. 16.

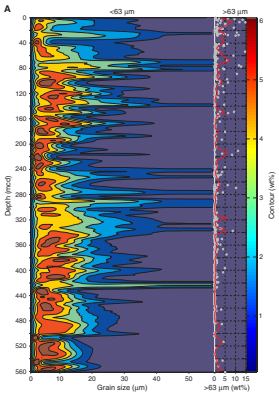

In general, the grain-size distribution downcore shows significant variations (Fig. **F6**). There are five prominent intervals in which cyclicity and the clay/silt ratio change drastically: (1) between 0 and 40 mcd (0 and 1.3 Ma), (2) between 40 and 80 mcd (1.3 and 2.4 Ma), (3) between 80 and 220 mcd (2.4 and 6 Ma), (4) between 220 and 360 mcd, and (5) below 360 mcd (prior to 8.1 Ma).

Interval 1 is characterized by small-scale variations and a pronounced dominance of the 5-µm size class fraction compared to the other identified intervals. Even though the overall grain-size distribution within this interval is very fine, interval 1 is also associated with a continuous tail of 1% of the distribution reaching the 40-µm fraction.

Interval 2 shows a steady increase in the dominant grain-size class and only small-amplitude cyclic variations. Interval 2 terminates with the highest dominant grain-size classes with 20 to 40 µm and 5% loading of our data set. The steady increase toward these highest recorded values seems to be interrupted between 60 and 70 mcd (~2.3 Ma). We attribute this gap in the temporal and spatial continuity of the grain-size distribution to the hiatus (discussed in Hillenbrand and Ehrmann, **Chap. 8,** this volume).

Interval 3 is characterized by very high amplitude and frequency cyclic distribution changes and a more or less steady decline in the grain-size mode and overall amplitude. High loadings of up to 4% for the 20-

µm window are reached in the middle of this interval at 135 mcd (4.3 Ma).

Interval 4, ~220 mcd (6 Ma), starts with a very narrow spectral distribution combined with high loadings of 6% in the size class below 5 µm. This nearly symmetrical upper zone of interval 4 has no tails into the coarser class fractions. The remaining lower part of the interval is characterized by a steady increase toward coarser size classes and moderately frequent but high-amplitude variability, especially in the coarser tail (>25 µm) of the grain-size spectra.

Interval 5, starting at ~360 mcd (8.1 Ma), shows the same cyclic pattern as interval 4, but with a decreasing trend in the occupied size classes.

The plot (Fig. F6) allows us also to check if the fine fraction (<63 µm) is locally affected by ice-rafted debris (IRD) events. These are suspected where the <63-µm fraction tails seem to be connected to peaks of the >63-µm fraction. (see Cowen, **Chap. 10,** and Wolf-Welling et al., **Chap. 15,** both this volume, for further IRD and coarse-fraction data).

Mean (1st moment)

$$\bar{x}_\phi = \Sigma f \cdot m/N,$$

Standard Deviation (2nd moment)

$$\sigma_\phi = \mathrm{SQR}[\Sigma f(m - \bar{x}_\phi)^2/100],$$

Skewness (3rd moment)

$$\mathrm{Sk}_\phi = \Sigma f(m - \bar{x}_\phi)^3/100\sigma_\phi^3, \text{ and}$$

Kurtosis (4th moment)

$$\mathrm{K}\phi = \Sigma f(m - \bar{x}_\phi)^4/100\sigma_\phi^4,$$

where

f = weight percent (frequency) in each grain-size grade present,
m = midpoint of each grain-size grade (in ϕ values), and
N = total number in sample; 100 when f is in percent.

For further general investigations, we applied the method of moments for the <63-µm data set. The weight percent of the fine fraction was hereby recalculated to 100%. The method of moments is well established (Griffith, 1967; Folk, 1974; Boggs, 1987) and is the mathematical expression of four characteristics of a quasi-Gaussian distribution. In this case, the moments are calculated using ϕ values. The skewness (third moment) and kurtosis (fourth moment) express the deviation of a grain-size frequency distribution from the general assumption of log normality to the base of two (Friedman, 1962). The results for the <63-µm range are given in a filtered (zero-phase low-pass filter) (Fig. F7) and discrete versions (Fig. F8). The filter has been applied after interpolating the data to constant depth and age resolution. The aim of this filtering procedure was to reduce the effects of uneven sampling spacing. A documentation of the frequency response and the resolution in time and distance of the

F7. Frequency response and resolution the filter algorithm, p. 18.

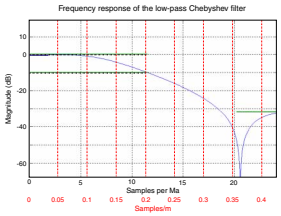

F8. Statistical grain-size data for the <63-µm data set, p. 19.

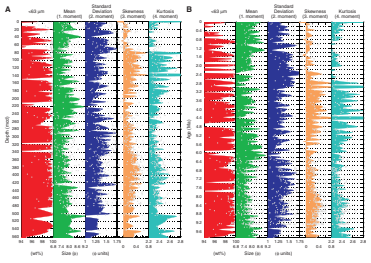

Chebyshev filter algorithm (Rabiner and Gold, 1975) used is given in Figure F7.

Particle-size data are presented as downhole plots vs. depth and age of bulk <63-µm fraction in weight percent of the total dry sample mass, mean (first moment), standard deviation (second moment), skewness (third moment), and kurtosis (fourth moment). Bulk fine-fraction contents are generally high (>95 wt%). The mean of the bulk fine fraction (<63 µm) varies between 7 and 9.2 ϕ units. There are some prominent maxima around 80 mcd (2.8 Ma), 138 mcd (4.4 Ma), 250 mcd (6.2 Ma), 290 mcd (6.8 Ma), 340 mcd (7.8 Ma), and 420 mcd (8.8 Ma). It appears that the mean of the fine fraction (<63 µm) is generally decoupled from the coarse fraction. Only in two cases, at 340 mcd (7.8 Ma) and 70 mcd (2.27 Ma), does a high mean of the coarse fraction correlate with a higher content of coarse fraction (>63 µm). Average standard deviation values above 1 ϕ indicate poor sorting of the <63-µm fraction (Folk, 1974). The standard deviation and mean of the fine fraction in ϕ units are inversely correlated throughout our data set. A decrease in degree of sorting is apparently coupled with higher mean grain-size values. The skewness values vary between –0.2 and >2. The skewness is, with a few exceptions, positive. This means that almost all samples analyzed have excess fine particles with respect to a log normal Gaussian distribution. There is a positive correlation between the skewness values and the kurtosis values. Fluctuations within the kurtosis values (measure of the peakness of a distribution) indicate highly variable depositional processes (Friedman, 1967).

The initially defined intervals, based on the overall appearance of the grain-size distributions in contour representation, also show distinguishing features in their moment representation. A detailed description is beyond the scope of this report, but some marked changes are noteworthy (e.g., the change in skewness and kurtosis between interval 2 and 3 or the time around 6 Ma [end of interval 3 and beginning of interval 4], where mean grain sizes reach a minimum that is combined with moderate sorting and low skewness and kurtosis values).

Not all of the <63-µm fraction is equally meaningful for the evaluation of depositional energy or paleocurrents. The special importance of grain-size parameters such as the sortable silt fraction (10–63 µm) as a percentage of the fine fraction (McCave, 1995a, 1995b), and the mean of the 10–63-µm fraction (McCave, 1995a) are especially current sensitive. Therefore, we applied the same statistical treatment (method of moments) to the sortable silt fraction (10–63 µm). Sortable silt fraction mean (first moment), standard deviation (second moment), skewness (third moment), and kurtosis (fourth moment) are presented as downhole plots vs. depth and age (Fig. F9). The data presented are unfiltered and uninterpolated to give a better idea of data density and data gaps. Sortable silt fraction values are generally much lower (average ~30 wt% of the fine fraction) than the bulk fine-fraction values, emphasizing the large fraction of <10-µm sediment not accounted for (Fig. F9; left column). In addition, the amplitude of fluctuation in the sortable silt fraction (10–63 µm) appears to be much higher in older sediments (below 280 mcd [late Miocene]). However, this may be the effect of higher sample density in this interval. The mean of the sortable silt fraction indicates that most of the sortable silt fraction has a grain size of ~6 ϕ units (15 µm), whereas the minimal mean values range below 5.4 ϕ units (25 µm).

As a result of removing the fine-grained tail below 10 µm, most of the skewness values turned negative in the sortable silt statistic. After

F9. Statistical grain-size data for the sortable silt fraction, p. 21.

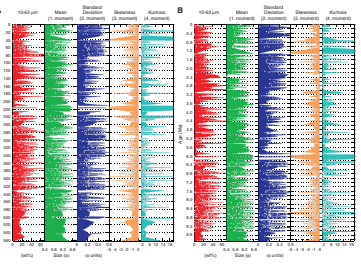

this modification, frequency distributions that originally had a nearly symmetrical distribution appear to be coarsely skewed.

Data Populations

Assuming that grain-size characteristics in the sortable silt range reflect conditions of the depositional process or environment, we used the statistical parameters determined by the methods of moments (Fig. F7) to group our data set. In contrast to previous approaches (Friedmann, 1961, 1967, 1979) that apply environmental statistical analyses to distinguish depositional settings (e.g., beach from river sand), we used bivariant plots to define depositional processes within a single depositional environment.

The best spatial separation of our sediment drift data set is in the bivariant plots: mean vs. skewness (Fig. F10A) and standard deviation vs. skewness (Fig. F10B). Three clearly separated populations are seen. Population 1 is characterized by the highest absolute mean grain sizes and standard deviation (Fig. F10C). Population 2 shows high variability in skewness and only small variations in mean grain size and standard deviation (Fig. F10A, F10B). Population 3 is characterized by the lowest mean and standard deviation values but displays the highest combined variability for the parameters skewness and standard deviation within the bivariant field (Fig. F10B, F10C). In general, samples with larger mean grain sizes have a higher standard deviation in our data set (Fig. F10C).

For a further visual inspection of the described populations we calculated average grain-size distributions for each population of the sortable silt (Fig. F11A) and for the <63-µm fraction (Fig. F11B). On average, populations 2 and 3 follow a unimodal distribution. In contrast, the average distribution of population 1 is very broad and bimodal. The average distribution plot for the sortable silt fraction (Fig. F11A) illustrates the characteristics of the three populations in a more graphical way.

DISCUSSION

The bimodal distribution of population 1 may indicate that the group actually consists of two populations. Figure F10B would allow definition of second population in this group. However, for the following discussion use populations 1–3 as defined in the data population section.

To check the significance of the populations for interpretation in terms of depositional processes, we plotted the data groups with their mean grain size against depth and age (Fig. F12). Blank areas within the first column indicate areas of no sample coverage. The mean of the grain-size populations correlates in general with the depositional energy of a system or depositional process. An arbitrarily chosen definition of the populations led to a random downhole distribution. Instead, the populations show distinct groups of spatial and temporal occurrence and absence. Population 1 is most common in four distinct time/depth intervals (intervals 1, 2, 4, and 5). Populations 2 and 3 are more continuous, except that population 3 is less common in younger/shallower deposits.

Our tentative correlation with depositional environments has been drawn from a comparison to a sequence stratigraphic model developed on board the ship (see “Lithostratigraphy” in Shipboard Scientific Party,

F10. Bivariant discrimination plots of statistical parameters, p. 23.

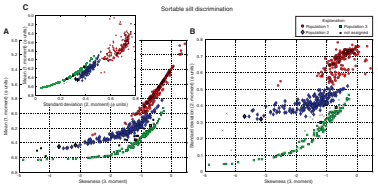

F11. Calculated average grain-size distributions, p. 24.

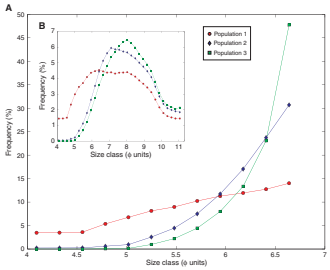

F12. Downhole plots of the three sortable silt populations, p. 25.

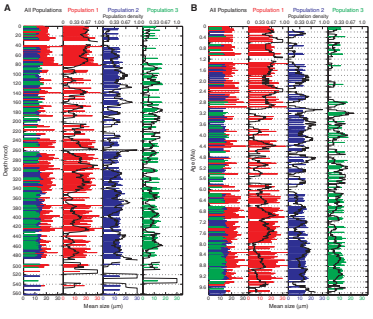

1999b). Population 3 is clearly related to bioturbated upper sequence boundaries that may be influenced by contourite currents. Population 1 is certainly glacial, with its maximum values correlating to ice-rafting events. However, most of population 1 may be indirectly ice-derived shelf material redeposited by turbidites. Especially noteworthy is the low number of population 1 events around 3–6 Ma, a global warm period (e.g., Messinian salinity crisis).

The depositional significance of population 2 is less certain; we assume an interglacial turbiditic origin. The density curves in Figure F12 represent counts of events at a certain depth and age ranges normalized to the total number of samples analyzed within this interval. The density curve of the glacial population 1 may therefore potentially be linked to parameters such as ice volume, shelf ice extent, or periods of advance and retreat of ice sheets.

CONCLUSIONS AND ONGOING WORK

This paper presents the laser diffraction–derived fine-fraction grain-size data for 530 samples from drift Site 1095. Contour techniques and the method of moments describe and characterize the frequency distribution data. The data set exhibits intervals of distinct changes in frequency, amplitude, and spatial (downcore) and temporal occurrence.

On the basis of three statistical parameters (mean, standard deviation, and skewness) calculated using the method of moments, it is possible to divide the data sets into at least three populations. The downcore and temporal distributions of the populations may be linked to discrete depositional processes.

Further investigations and the incorporation of other data sets are needed for definitive statements toward a new sequence stratigraphic model for Drift 7. In our ongoing project, the bivariant approach for discriminating the data set will be tested against multivariant factor and cluster analysis and complex physical properties based depositional models.

ACKNOWLEDGMENTS

This research used samples and/or data provided by the Ocean Drilling Program (ODP). ODP is sponsored by the U.S. National Science Foundation (NSF) and participating countries under management of Joint Oceanographic Institutions (JOI), Inc. Funding for this research was provided by SPP DSDP/ODP grants TH 200/37-1 and -2 from the Deutsche Forschungsgemeinschaft.

Thanks to our spouses and children for letting us go and for spending their time to improve this paper. Extraordinary merits have been earned by Giorgio Fontolan from the University at Trieste, Italy, through his thoughtful review and commitment to improve the paper.

Special thanks also to Prof. W. Hay, Dr. Warner Brückmann, Daniel A. Hepp, Jayne Welling-Wolf, and Ortrud Runze for early reviews of the paper.

REFERENCES

Andersen, J.U., 1963. An improved pretreatment for mineralogy analysis of samples containing organic matter. *Clays and Clay Minerals,* 10:380–388.

Barker, P.F., 1995. The proximal marine sediment record of Antarctic climate since the late Miocene. *In* Cooper, A.K., Barker, P.F., and Brancolini G. (Eds.), *Geology and Seismic Stratigraphy of the Antarctic Margin.* Am. Geophys. Union, Antarct. Res. Ser., 68:25–57.

Barker, P.F., Barrett, P.J., Camerlenghi, A., Cooper, A.K., Davey, F.J., Domack, E.W., Escutia, C., Kristoffersen, Y., and O'Brien, P.E., 1998. Ice sheet history from Antarctic continental margin sediments: the ANTOSTRAT approach. *Terra Antart.,* 5:737–760.

Barker, P.F., Barrett, P.J., Cooper, A.K., and Huybrechts, P., 1999. Antarctic glacial history from numerical models and continental margin sediments. *Palaeogeogr., Palaeoclimatol., Palaeoecol.,* 150:247–267.

Boggs, S., Jr., 1987. *Principles of Sedimentology and Stratigraphy:* New York (Macmillan).

Camerlenghi, A., Crise, A., Pudsey, C.J., Accerboni, E., Laterza, R., and Rebesco, M., 1997. Ten-month observation of the bottom current regime across a sediment drift of the Pacific margin of the Antarctic Peninsula. *Antarct. Sci.,* 9:426–433.

Folk, R.L., 1974. *Petrology of Sedimentary Rocks:* Austin, TX (Hemphill Publ.).

Friedman, G.M., 1961. Distinction between dune, beach, and river sands from their textural characteristics. *J. Sed. Petrology,* 31:514–529.

————, 1962. On sorting, sorting coefficients, and the log normality of the grain-size distribution of sandstones. *J. Geol.,* 70:737–753.

————, 1967. Dynamic processes and statistical parameters compared for size frequency distribution of beach and river sands. *J. Sed. Petrology,* 37:327–354.

————, 1979. Address of the retiring President of the International Association of Sedimentologists: differences in size distributions of populations of particles among sands of various origins. *Sedimentology,* 26:3–32.

Fritsch GmbH Laborgerätebau, 1994. *Benutzer-Handbuch Laser Partikel Sizer "analysette 22":* Idar-Oberstein (Fritsch GmbH Laborgerätebau).

Griffith, J.C., 1967. *Scientific Methods in Analysis of Sediments:* New York (McGraw-Hill).

Matthews, M.D., 1991. The effect of pretreatment on size analysis. *In* Syvitski, J.P.M. (Ed.), *Principles, Methods, and Application of Particle Size Analysis:* Cambridge (Cambridge University Press), 34–42.

McCave, I.N., Bryant, R.J., Cook, H.F., and Coughanowr, C.A., 1986. Evaluation of a laser-diffraction-size analyzer for use with natural sediments. *J. Sediment. Petrol.,* 56:561–564.

McCave, I.N., Manighetti, B., and Beveridge, N.A.S., 1995a. Circulation in the glacial North Atlantic inferred from grain-size measurements. *Nature,* 374:149–151.

McCave, I.N., Manighetti, B., and Robinson, S.G., 1995b. Sortable silt and fine sediment size/composition slicing: parameters for palaeocurrent speed and palaeoceanography. *Paleoceanography,* 10:593–610.

Rabiner, L.R., and Gold, B., 1975. *Theory and Application of Digital Signal Processing:* Englewood Cliffs, NJ (Prentice-Hall).

Rebesco, M., Camerlenghi, A., and Zanolla, C., 1998. Bathymetry and morphogenesis of the continental margin west of the Antarctic Peninsula. *Terra Antart.,* 5:715–728.

Shipboard Scientific Party, 1999a. Leg 178 summary. *In* Barker, P.F., Camerlenghi, A., Acton, G.D., et al., *Proc. ODP, Init. Repts.,* 178: College Station TX (Ocean Drilling Program), 1–60.

————, 1999b. Site 1095. *In* Barker, P.F., Camerlenghi, A., Acton, G.D., et al., *Proc. ODP, Init. Repts.,* 178, 1–173 [CD-ROM]. Available from: Ocean Drilling Program, Texas A&M University, College Station, TX 77845-9547, U.S.A.

Von Bernuth, G., 1988. Laser-Partikel-Sizer "analysette 22:" Ein Labor- und Betriebsmessgerät Messung von Partikelgrössenverteilungen an mineralischen und synthetischen Rohstoffen. *TIZ,* 5.

Figure F1. Bathymetric map of the continental margin west of the Antarctic Peninsula (Rebesco et al., 1998) with Site 1095 and 1096 locations on Drift 7 (solid circles). The approximate location of seismic line I95-137 is also indicated (red line).

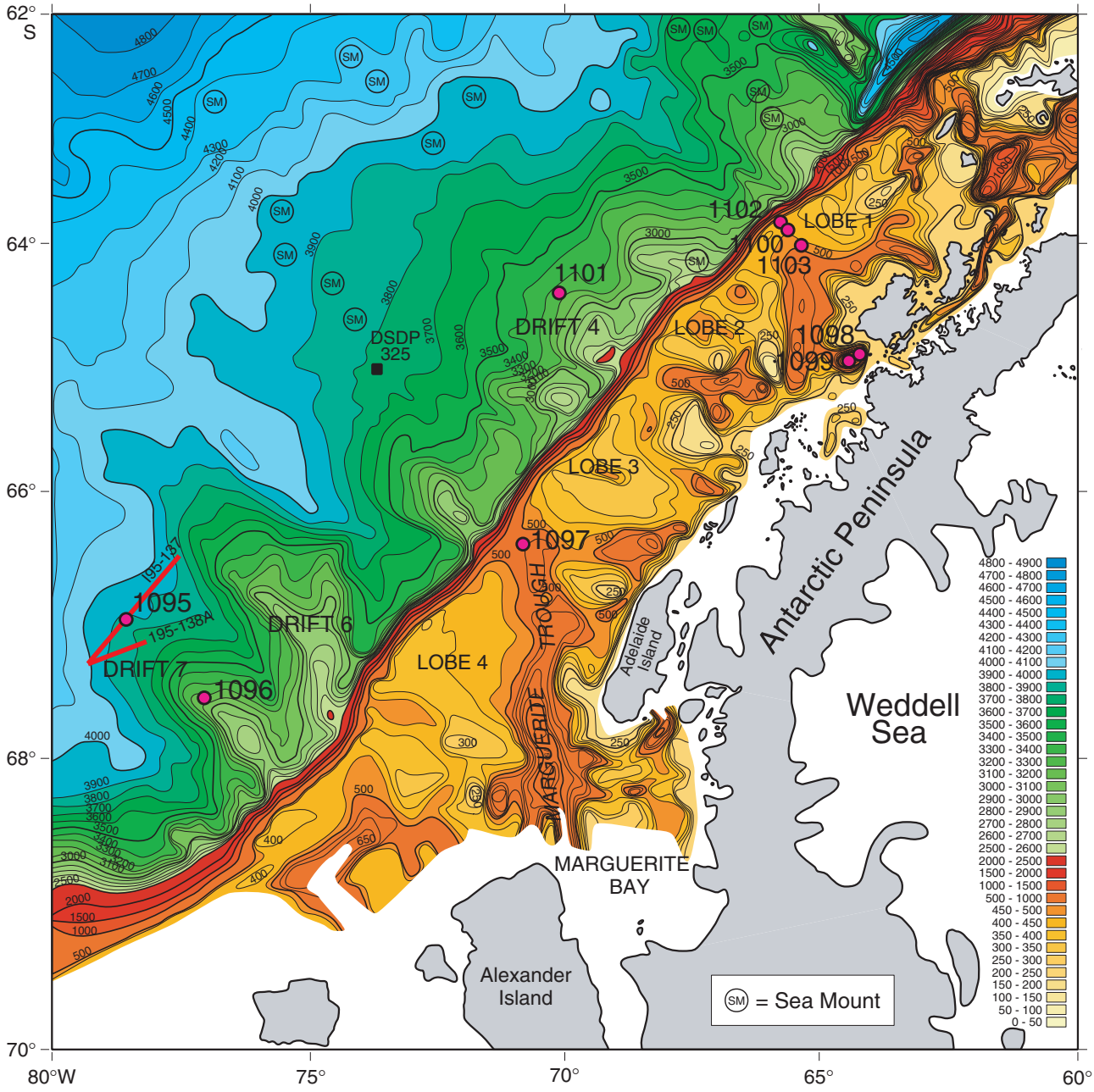

Figure F2. Southwest-northeast air gun multichannel reflection seismic profile across the seaward end of Drift 7 (for location, see caption of Fig. F1, p. 11). The profile crosses Site 1095 (Shipboard Scientific Party, 1999a). S.P. = shotpoint.

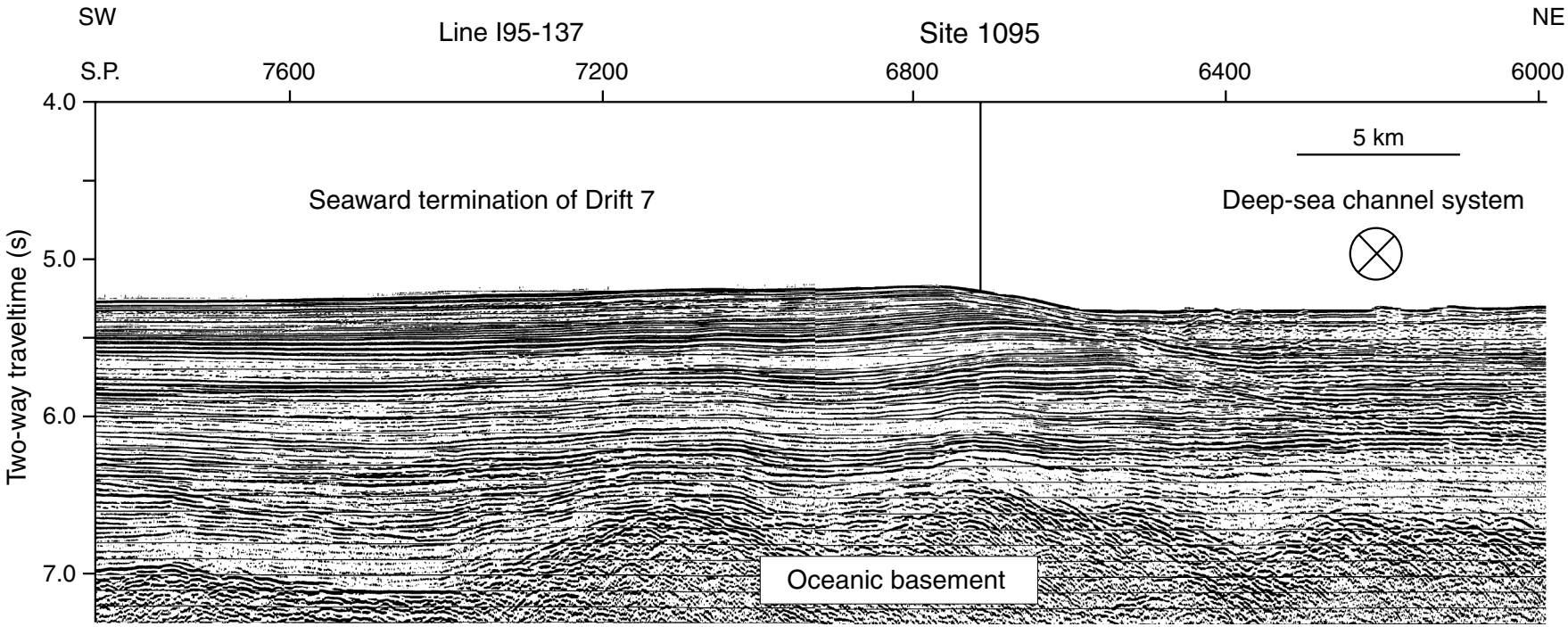

Figure F3. Sample preparation scheme. Long passing times are due to an abundant very fine clay portion with slow settling velocities.

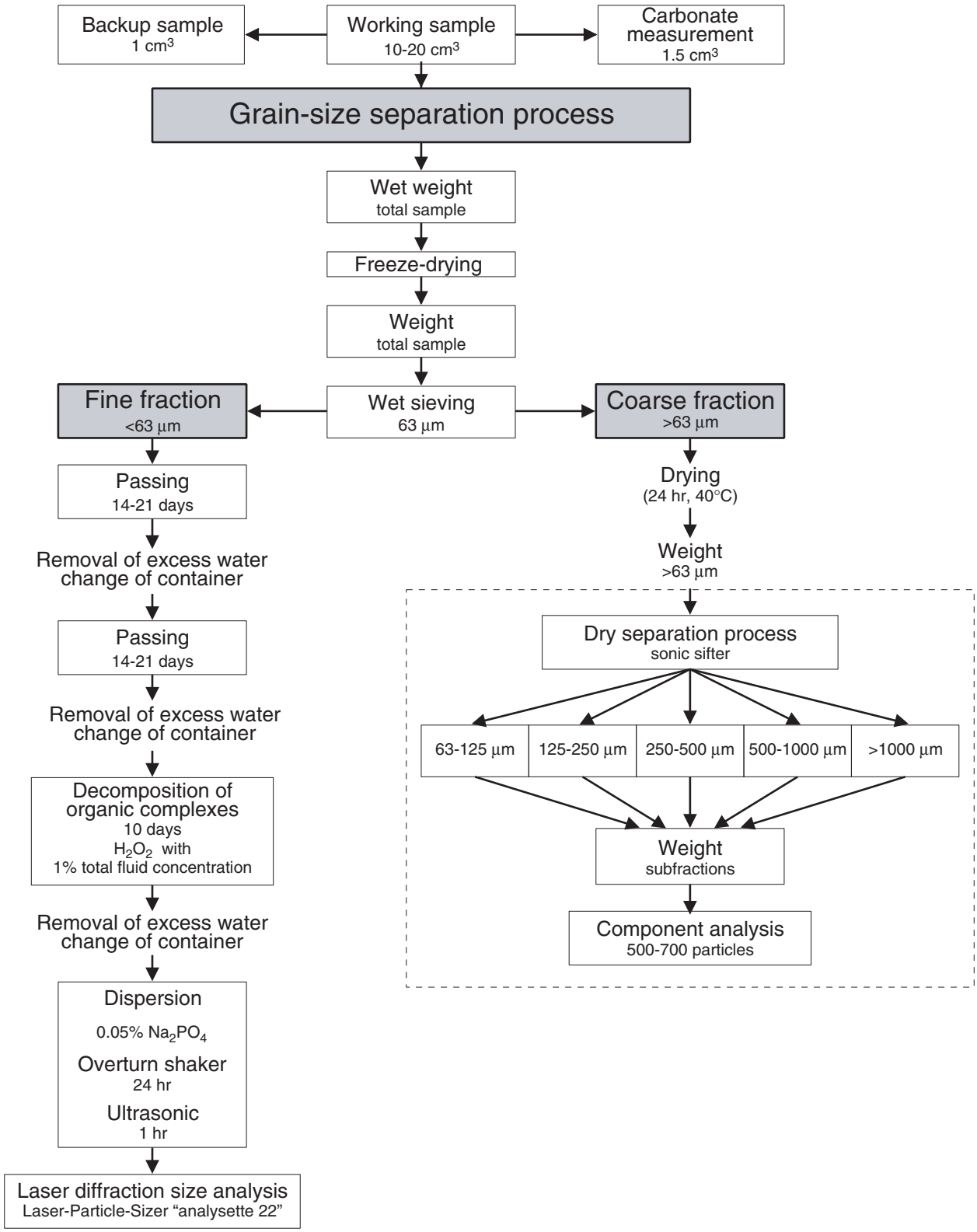

Figure F4. A. Layout of the laser particle sizer "Analysette 22"-Economy (Fritsch GmbH Laborgerätebau, 1994). The unit is equipped with a 632.8-nm wavelength and 3-mW helium-neon laser and handles suspensions with a particle size between 0.1 and 600 µm. **B, C.** The unique fixed focus size analyzing system with particle size range–dependent cell shift. Shifting the sampling cell relative to the detector changes the diffraction angle and the size of the sensor area affected. A large distance between sampling cell and detector therefore permits the measurement of larger particles with a smaller diffraction angle, and short distances are used for small particles with a wide diffraction angle.

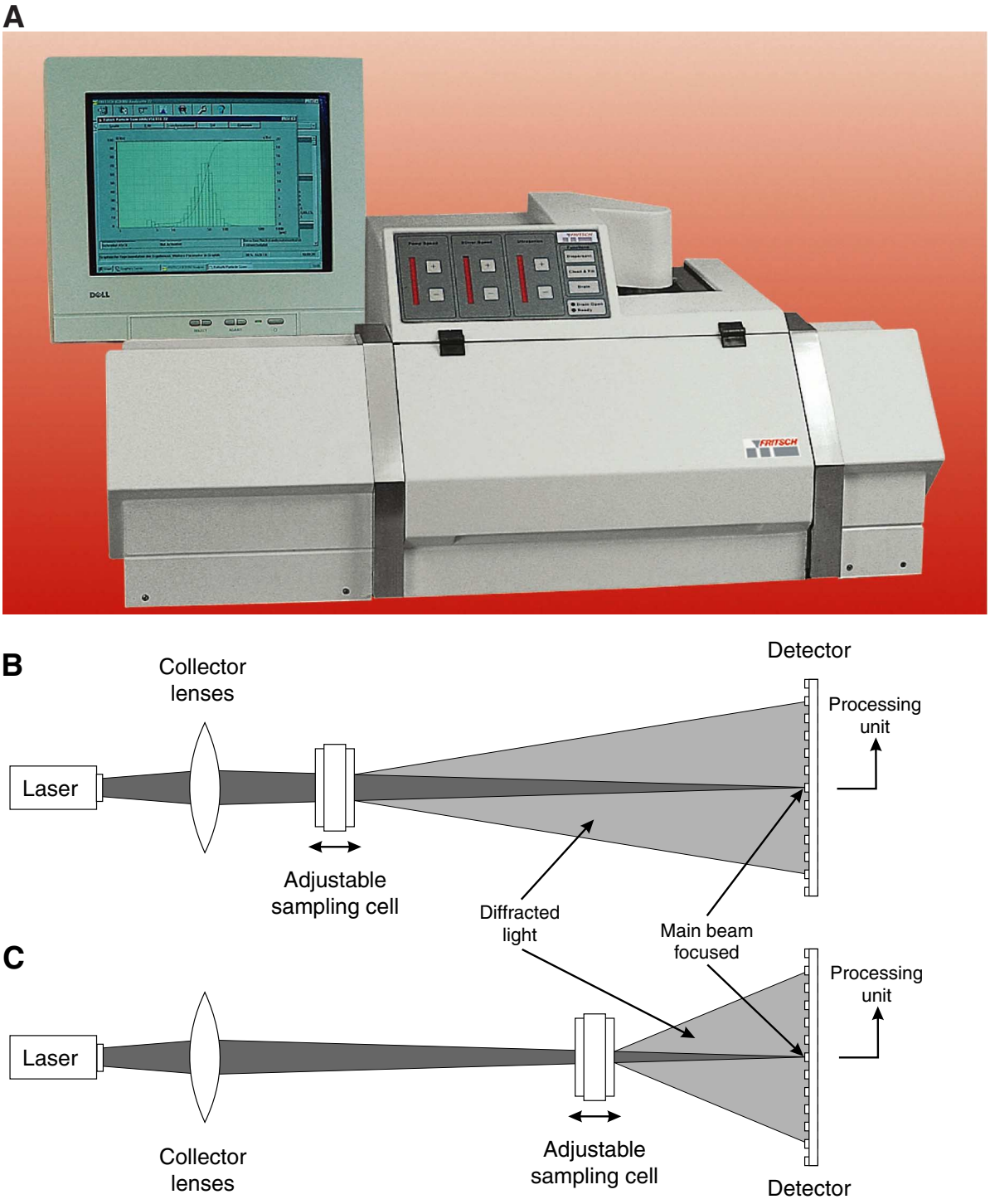

Figure F5. A. Size classes in millimeter and ϕ values. **B, C.** Differences in frequency spectra plots given in millimeter and ϕ values.

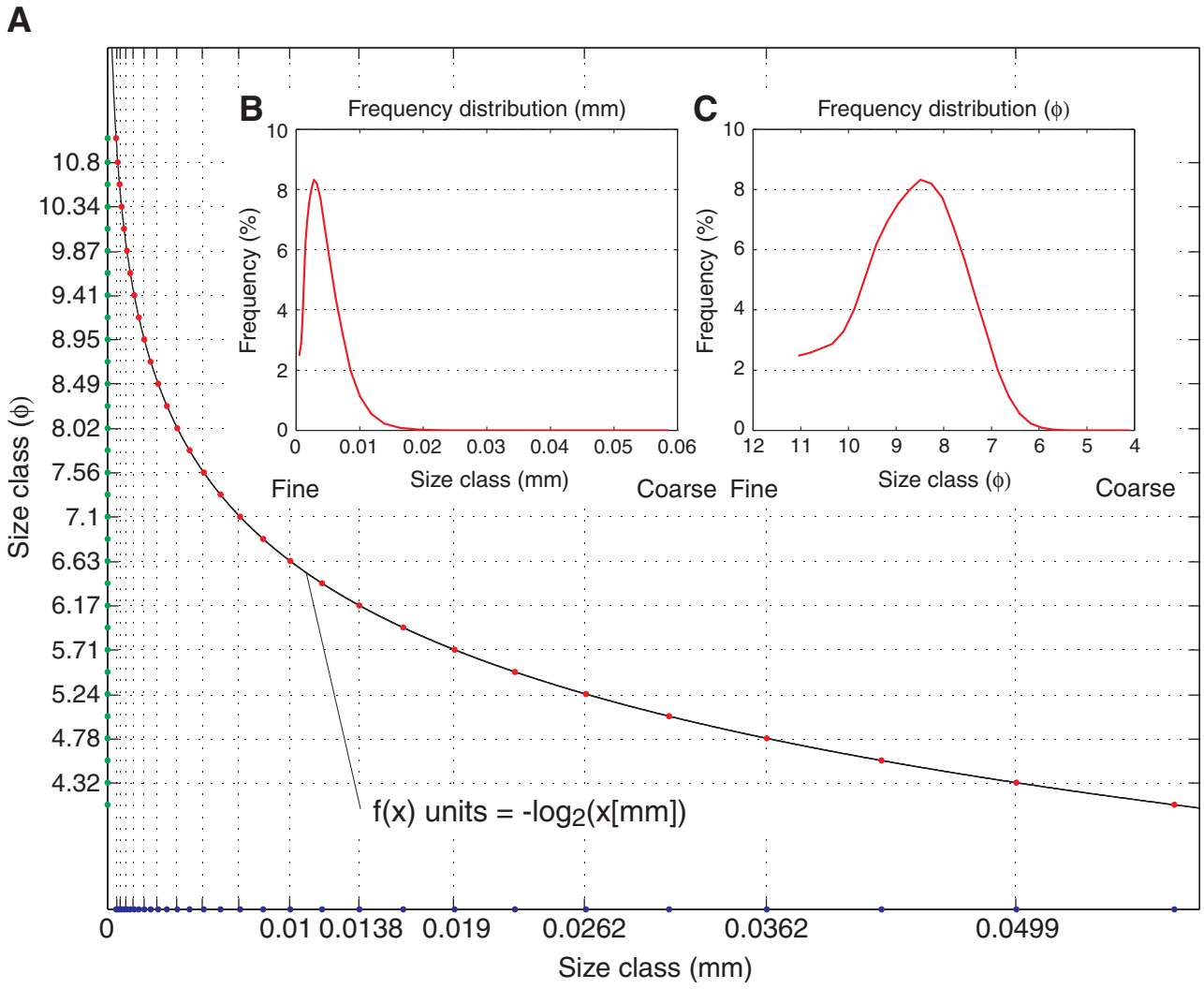

Figure F6. A. Contour plots of the fine-fraction data vs. depth. The contour algorithm chosen is linear and resolves six contour levels representing the percent of sediment found for each grain-size class. Percent values refer to the total sediment sample dry mass. The size fraction >63 µm was added as an undifferentiated two-dimensional summary curve as a separate column at the right side of the graph. Single data values and a zero-phase filtered curve are given for the >63-µm fraction. (Continued on next page.)

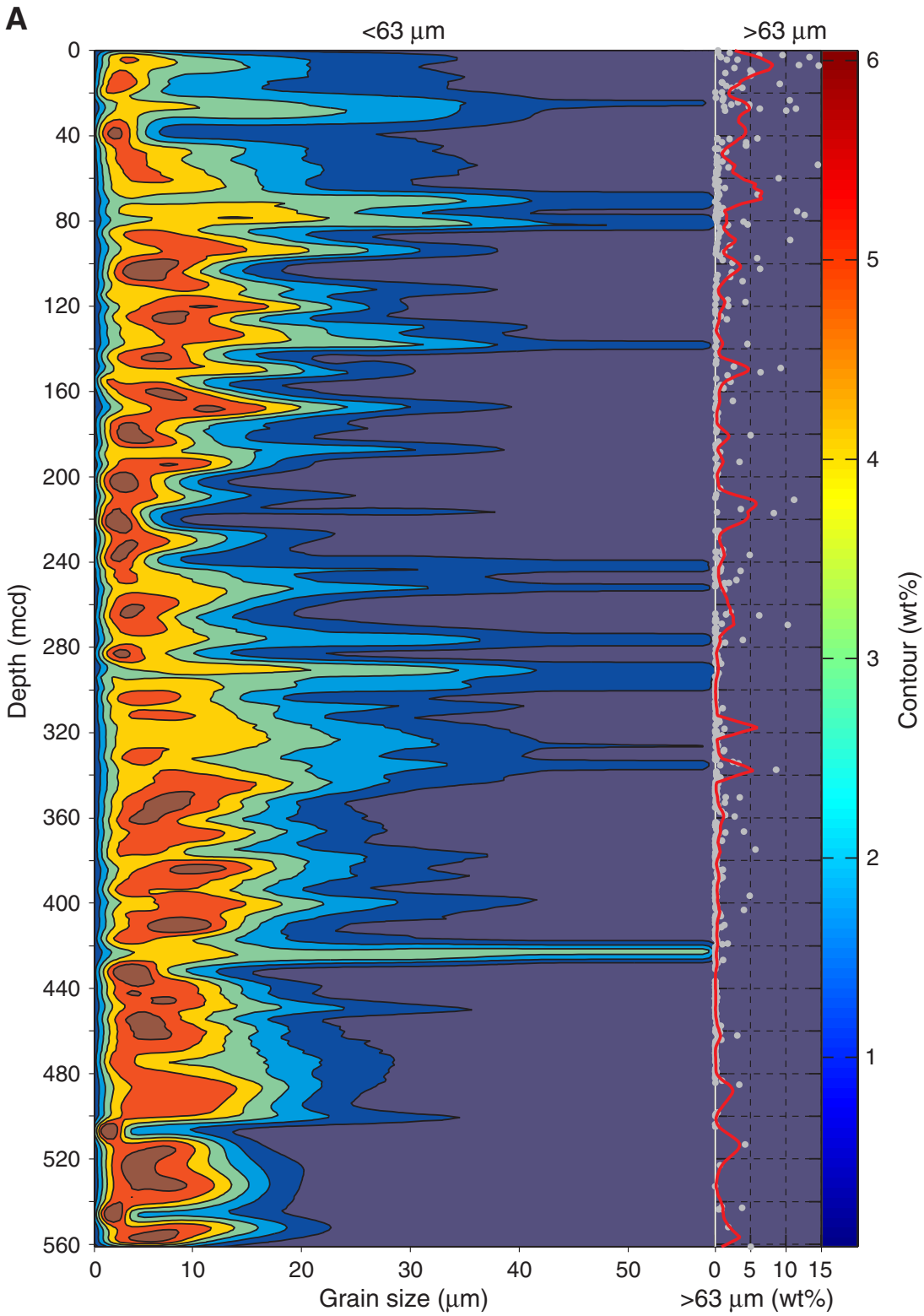

Figure F6 (continued). B. Contour plots of the fine-fraction data vs. age.

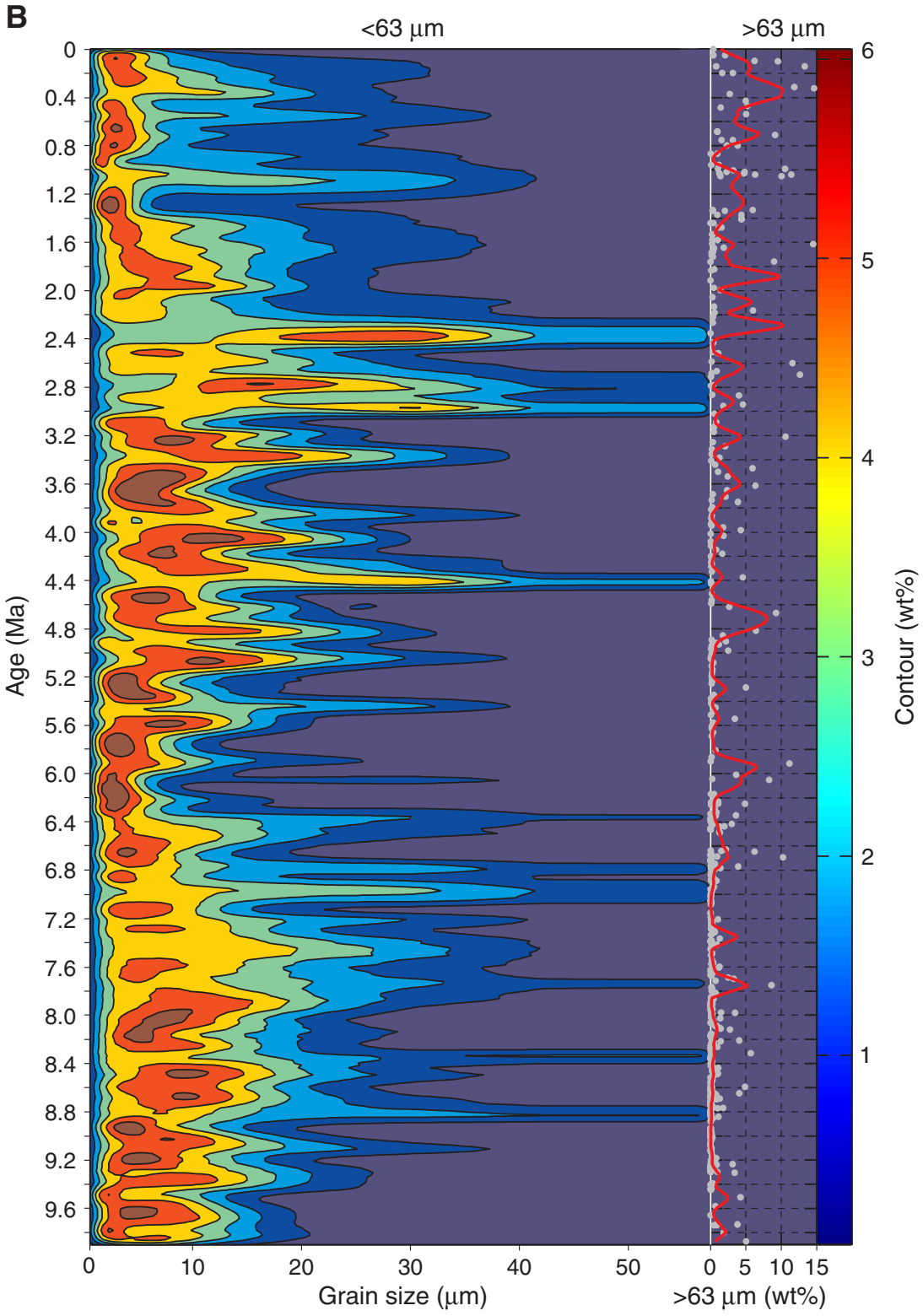

Figure F7. Frequency response and the resolution in time and distance of the Chebyshev zero-phase low-pass filter algorithm used to remove artificial high-frequency patterns resulting from unequal sample spacing.

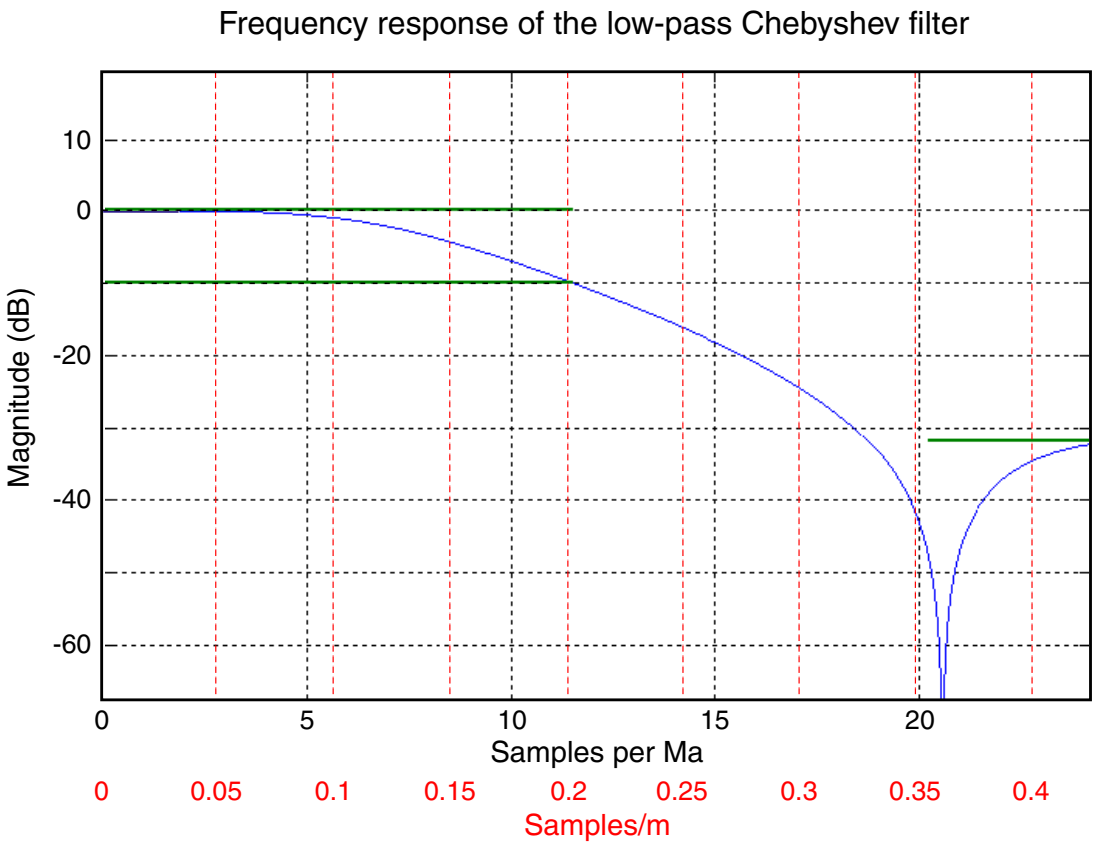

Figure F8. Statistical grain-size data using the method of moments for all of the <63-µm data set. The results are given in a low-pass filtered and discrete version vs. (**A**) depth and (**B**) age. Bulk fine-fraction contents are generally high (>95 wt%). (**Figure shown on next page.**)

Figure F8 (continued). (Caption shown on previous page.)

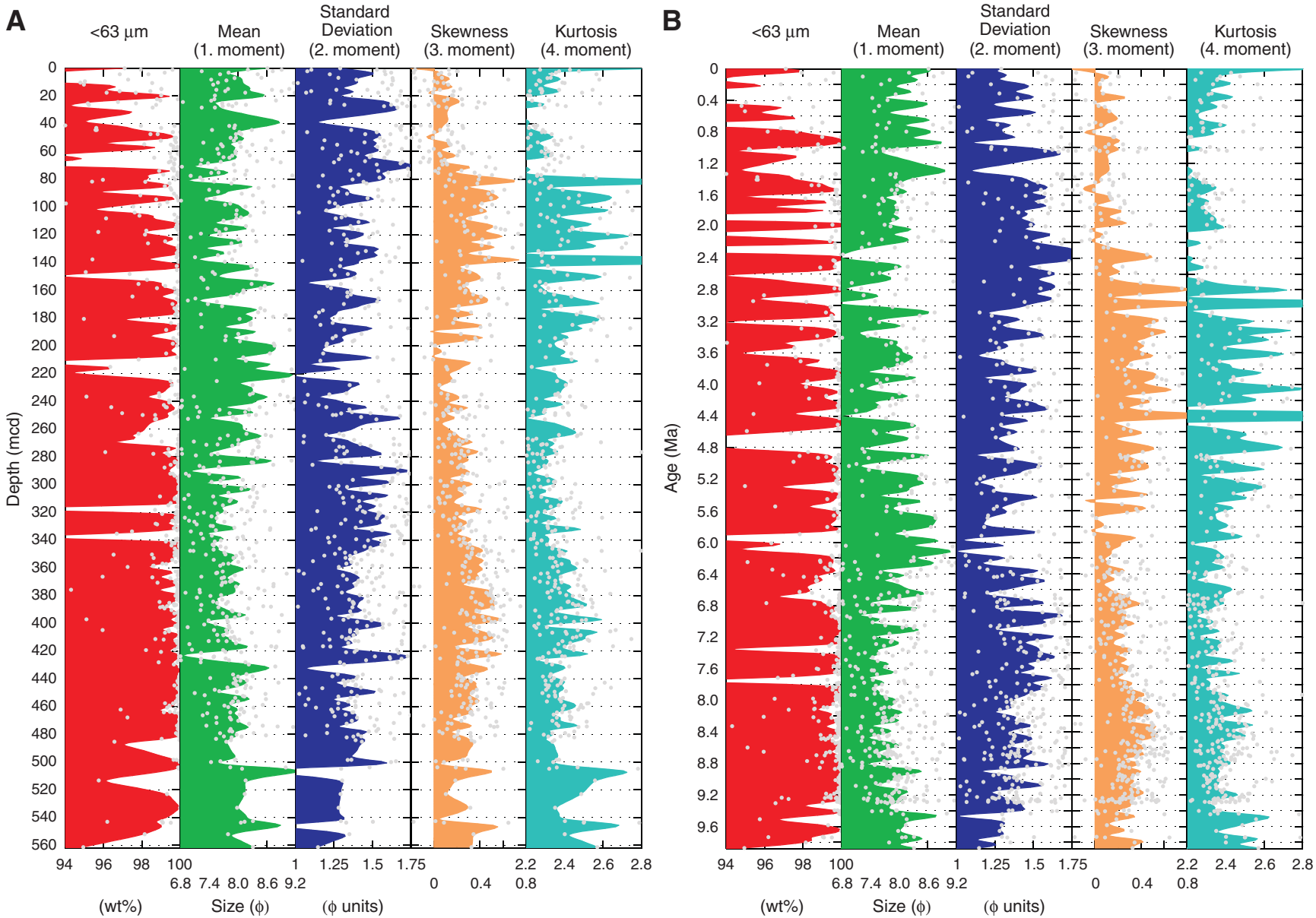

Figure F9. Statistical grain-size data using the method of moments for the sortable silt fraction (10–63 µm) of our data set. The results are given uninterpolated in discrete samples vs. (**A**) depth and (**B**) age. The amplitude of fluctuation of the statistical parameters in the sortable silt fraction is more pronounced than in the bulk fine-fraction data set. Note the unequal spacing of our data coverage. (**Figure shown on next page.**)

Figure F9 (continued). (Caption shown on previous page.)

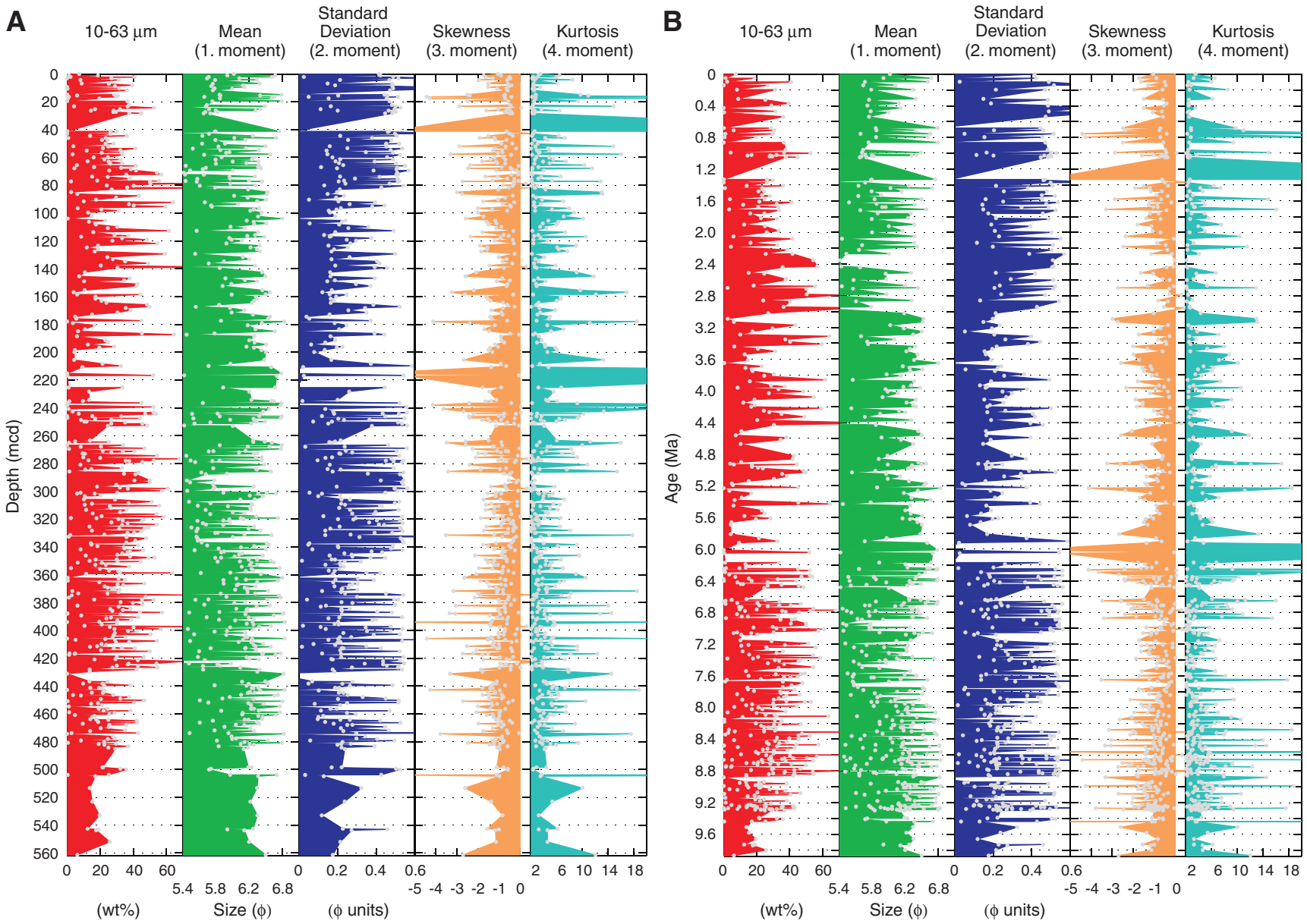

Figure F10. Bivariant discrimination plots of the statistical parameters (**A**) mean vs. skewness, (**B**) standard deviation vs. skewness, and (**C**) mean vs. standard deviation skewness leading to the definition of three distinct populations.

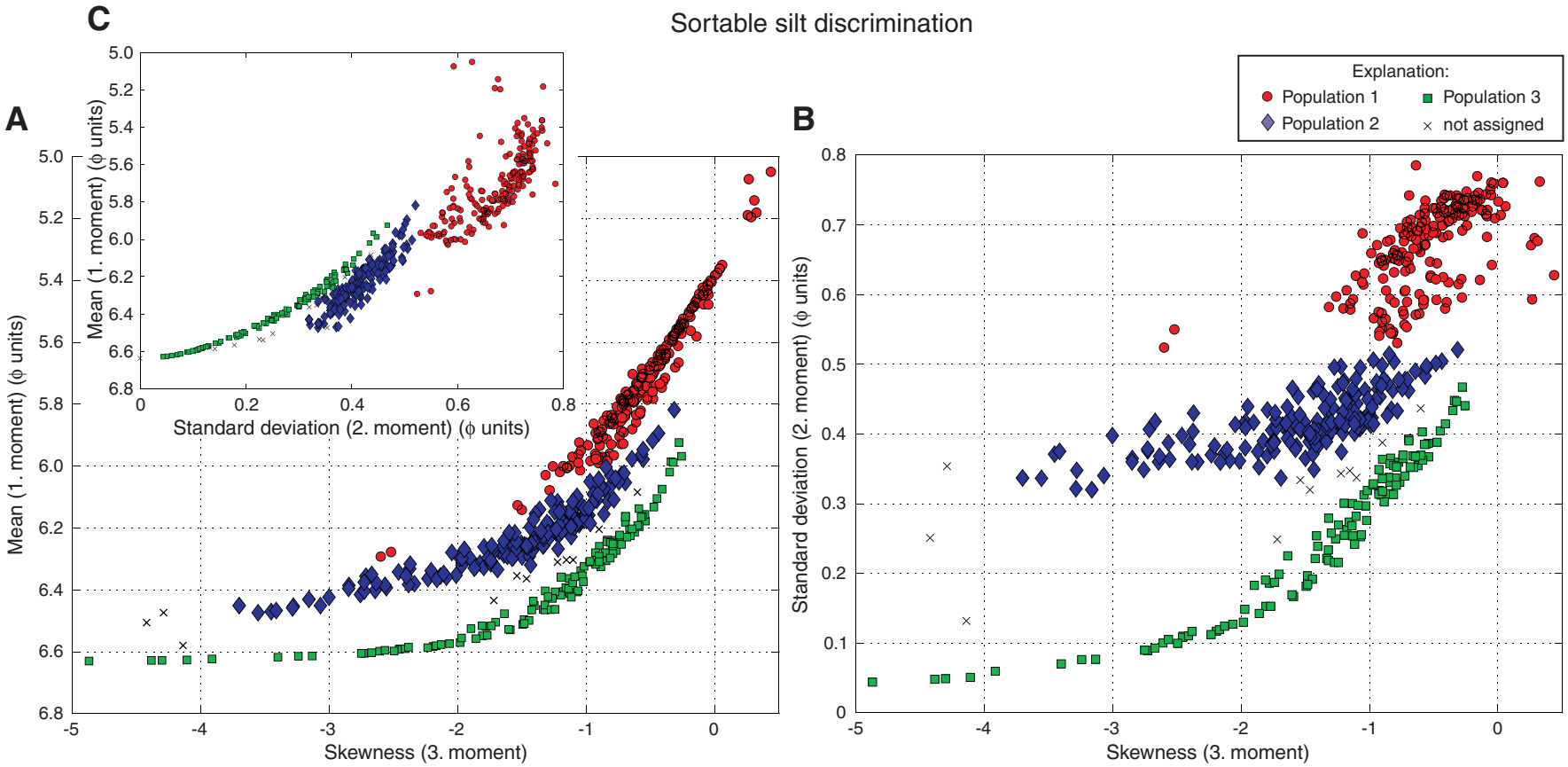

Figure F11. Calculated average grain-size distributions for each population of the (**A**) sortable silt and (**B**) <63-µm fraction. Populations 2 and 3 follow a unimodal distribution. Population 1 has a bimodal distribution, indicating that it may be further split in two subfractions.

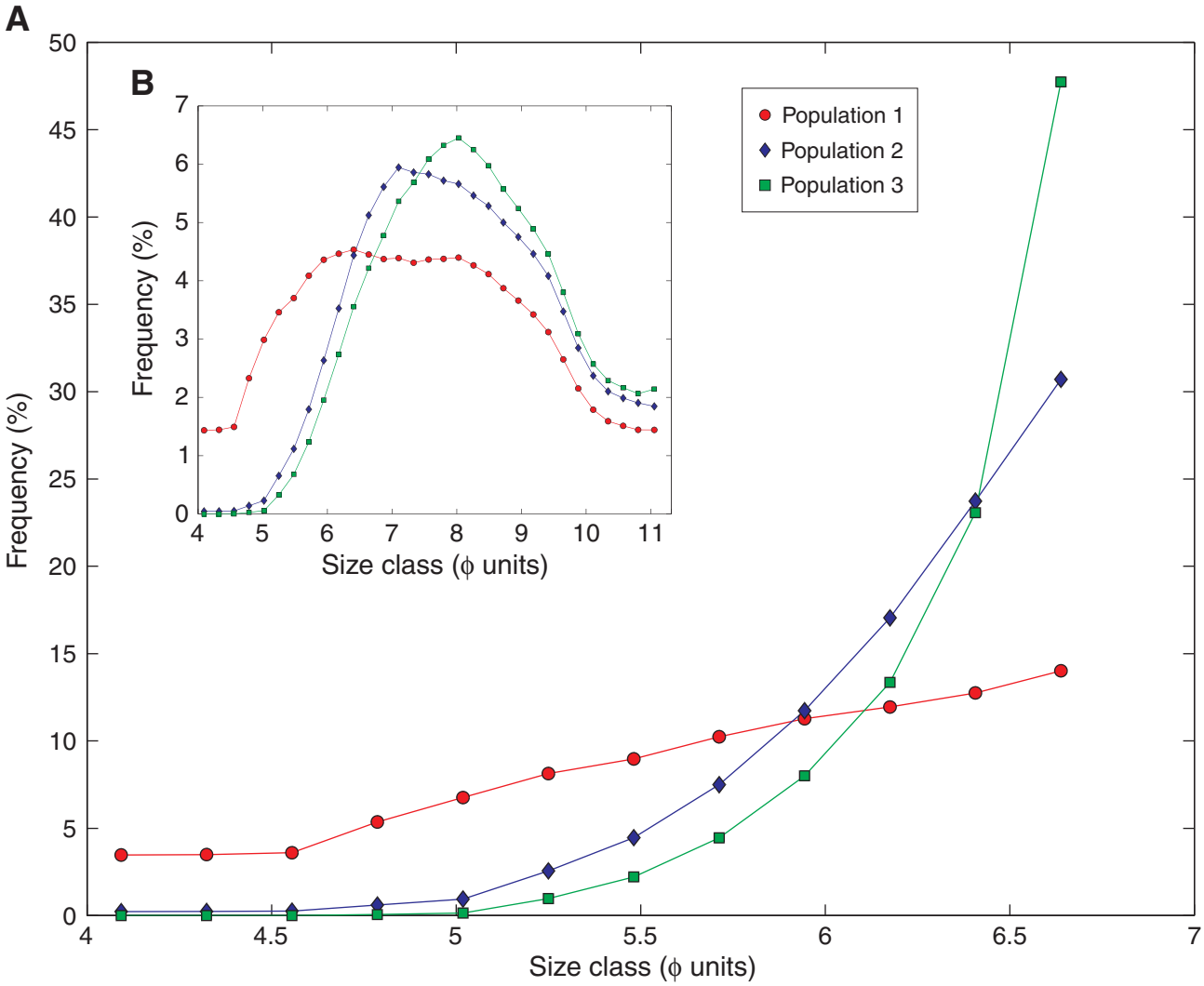

Figure F12. Downhole plots of the three sortable silt populations vs. (**A**) depth and (**B**) age. The populations are color coded, and the amplitude refers to the mean grain size. The black curves for each population represent the density of the occurrence of the specific population normalized to the total number of samples within a 10-m depth or 0.2-Ma time window. (**Figure shown on next page.**)

Figure F12 (continued). (Caption shown on previous page.)

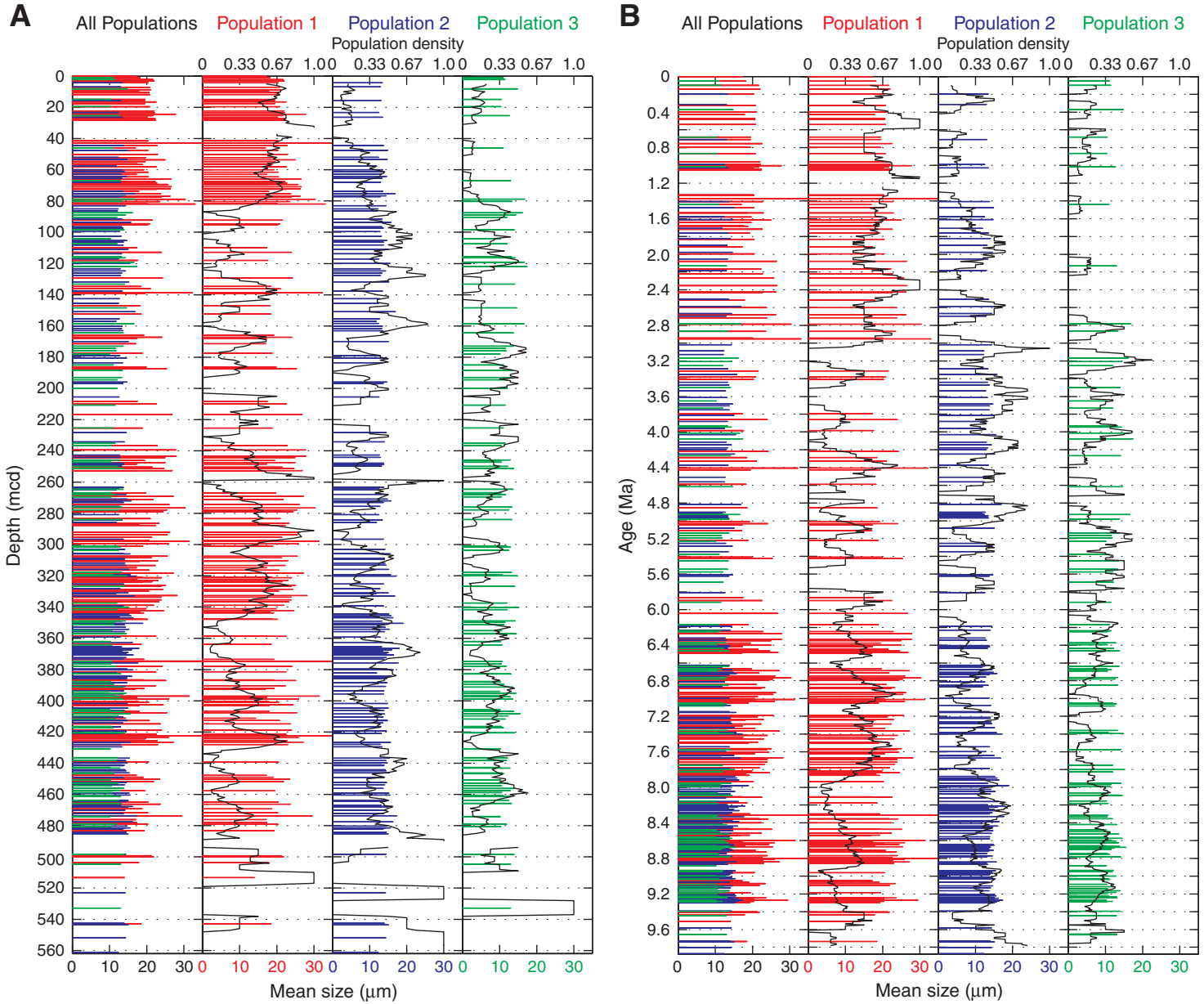

Table T1. Grain-size classes.

Midpoint (μm)	Midpoint (ϕ)	Lower (μm)	Upper (μm)
0.47	11.055	0.425	0.514
0.559	10.805	0.514	0.604
0.656	10.574	0.604	0.709
0.771	10.341	0.709	0.832
0.905	10.11	0.832	0.977
1.062	9.879	0.977	1.147
1.247	9.647	1.147	1.347
1.464	9.416	1.347	1.581
1.719	9.184	1.581	1.856
2.018	8.953	1.856	2.179
2.369	8.722	2.179	2.559
2.781	8.49	2.559	3.004
3.265	8.259	3.004	3.527
3.834	8.027	3.527	4.14
4.501	7.796	4.14	4.861
5.284	7.564	4.861	5.707
6.203	7.333	5.707	6.7
7.283	7.101	6.7	7.866
8.55	6.87	7.866	9.235
10.038	6.638	9.235	10.842
11.785	6.407	10.842	12.728
13.836	6.175	12.728	14.943
16.243	5.944	14.943	17.543
19.07	5.713	17.543	20.596
22.388	5.481	20.596	24.18
26.284	5.25	24.18	28.388
30.858	5.018	28.388	33.328
36.228	4.787	33.328	39.127
42.532	4.555	39.127	45.936
49.933	4.324	45.936	53.929
58.622	4.092	53.929	63.314

Notes: The size class ranges and midpoints for this study are taken directly from the analysette output files. As one reviewer noted, the midpoints are apparently calculated geometrically: class midpoint = (upper size class boundary + lower size class boundary)/2. A more sophisticated way to determine the midpoint of logarithmic spaced size class intervals would be, of course, the arithmetic mean: class midpoint = (upper size class boundary x lower size class boundary)1/2. However, we chose to use the machine output since the class spacing is small and any possible introduced error is negligible.